Supplemental Document

Biomedical Optics EXPRESS

The LUCA device: a multi-modal platform combining diffuse optics and ultrasound imaging for thyroid cancer screening: supplement

LORENZO CORTESE,[1,14,*] GIUSEPPE LO PRESTI,[1,14] MARTA ZANOLETTI,[2] GLORIA ARANDA,[3] MAURO BUTTAFAVA,[4] DAVIDE CONTINI,[2] ALBERTO DALLA MORA,[2] HAMID DEHGHANI,[5] LAURA DI SIENO,[2] SIXTE DE FRAGUIER,[6] FELICIA A. HANZU,[3,7,8] MIREIA MORA PORTA,[3,7,8] AN NGUYEN-DINH,[9] MARCO RENNA,[4,10] BOGDAN ROSINSKI,[9] MATTIA SQUARCIA,[3,11] ALBERTO TOSI,[4] UDO M. WEIGEL,[12] STANISLAW WOJTKIEWICZ,[5] AND TURGUT DURDURAN[1,13]

[1] *ICFO-Institut de Ciències Fotòniques, The Barcelona Institute of Science and Technology, 08860 Castelldefels (Barcelona), Spain*
[2] *Politecnico di Milano, Dipartimento di Fisica, 20133 Milano, Italy*
[3] *IDIBAPS, Fundació Clínic per la Recerca Biomèdica, Barcelona, Spain*
[4] *Politecnico di Milano, Dipartimento di Elettronica Informazione e Bioingegneria, 20133 Milano, Italy*
[5] *University of Birmingham, School of Computer Science, Edgbaston, Birmingham, B15 2TT, UK*
[6] *IMV Imaging, 16000 Angoulême, France*
[7] *Endocrinology and Nutrition Department, Hospital Clínic of Barcelona, Barcelona, Spain*
[8] *Centro de Investigación Biomèdica en Red Diabetes y Enfermedades Metabólicas Asociadas (CIBERDEM), Spain*
[9] *VERMON S.A., 37000 Tours, France*
[10] *Athinoula A. Martinos Center for Biomedical Imaging, MGH, Harvard Medical School, Charlestown, MA 02129, USA*
[11] *Neuroradiology Department, Hospital Clínic of Barcelona, Barcelona, Spain*
[12] *HemoPhotonics S.L., 08860 Castelldefels (Barcelona), Spain*
[13] *Institució Catalana de Recerca i Estudis Avançats (ICREA), 08015 Barcelona, Spain*
[14] *These authors equally contributed to this work. Authors are listed in alphabetical order except for the first three and the last*
[*] *lorenzo.cortese@icfo.eu*

This supplement published with The Optical Society on 14 May 2021 by The Authors under the terms of the Creative Commons Attribution 4.0 License in the format provided by the authors and unedited. Further distribution of this work must maintain attribution to the author(s) and the published article's title, journal citation, and DOI.

Supplement DOI: https://doi.org/10.6084/m9.figshare.14558703

Parent Article DOI: https://doi.org/10.1364/BOE.416561

Supplementary information - Section 3

3.3 TRS phantom characterization

BIP PROTOCOL:

The Basic Instrumental Performance (BIP) protocol aims to assess the fundamental quantities that affect the Instrument Response Function (IRF), which in turn reflects the accuracy of the measurements in clinical settings. The features that plays a key role in contributing to the temporal resolution of the device are the laser pulse shape, timing jitter of the detector electronics and, finally, the temporal dispersion through the fibres. The IRF is then the convolution of all these effects. Characterization guidelines were followed as in [1].

a. SOURCE COMPONENTS

Average power at the sample

The maximum optical power delivered to the sample (fully open attenuators) has been measured for all the lasers by means of an optical power meter (S140C, Thorlabs GmbH, Germany) placed at the end of the injection fibre tip. Powers ranging from 0.62 mW (at 730 nm) up to 2.90 mW (at 830 nm), are reported in Table 1.

Table 1 Maximum power injected into the sample/tissue as measured at the tip of the injection fiber.

	635	670	730	830	852	915	980	1040
P_{in} (mW)	1.70	2.64	0.62	2.90	2.37	2.51	2.07	2.89

b. DETECTION AND ACQUISITION CHAIN

Responsivity

Responsivity have been calculated as:

$$R_{det}(\lambda) = \frac{N_{tot}}{t_{meas} k_p(\lambda) P_{in}(\lambda)} \; [m^2 sr]$$

where N_{tot} is the total number of counts, t_{meas} is the integration time of the measurement (in this case 20 s) and $k_p(\lambda)$ is phantom-specific factor, which includes the transformation of the input power P_{in} into photon number. Measurements were performed by placing the injection fibre in contact with a calibration phantom (described in [1]) and by collecting light in transmittance modality for both the channels. Values of responsivity are shown in Figure 1.

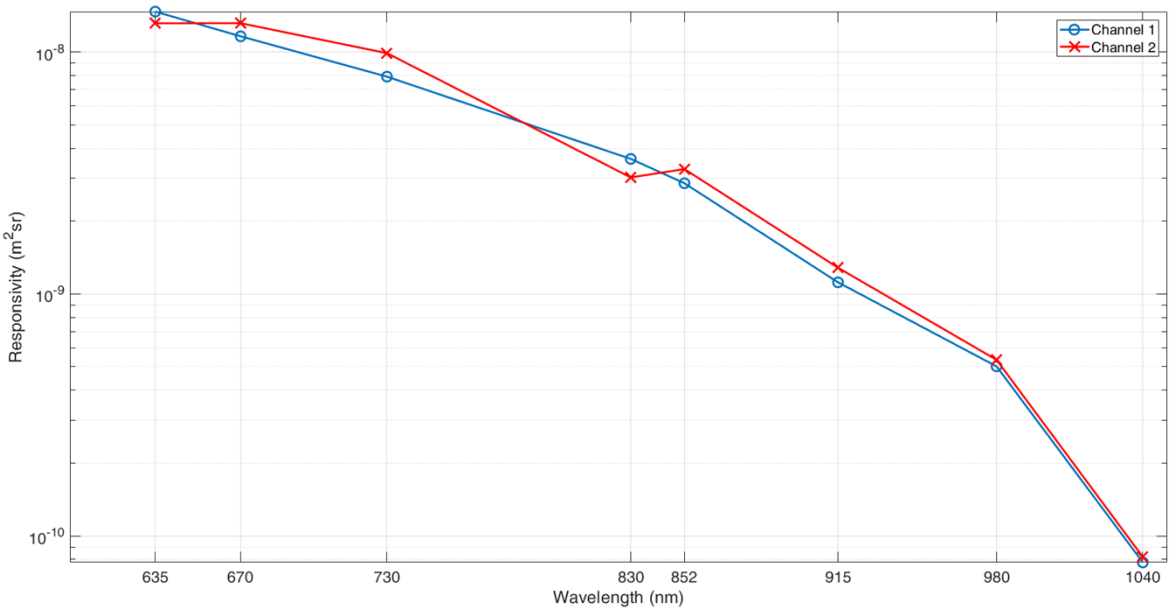

Figure 1 Responsivity calculated over the entire range of wavelengths of the LUCA system for both channel 1 and 2.

Differential non linearity

The quantification of the Differential Non Linearity (DNL) affecting the two TDCs is performed by shining uncorrelated light (from a LED torch) onto the SiPMs while hitting a target count rate of about $1 \cdot 10^6$ counts per second, as shown in the Figure 2. Histograms are acquired 10 times with an integration time of 10 s per repetition. Finally, as defined in the BIP protocol, DNL is computed by the following equation, which represents the peak-to-peak difference normalized to the mean value:

$$\epsilon_{DNL}(\%) = \frac{N_{DNL,MAX} - N_{DNL,MIN}}{\overline{N_{tot}}} \cdot 100.$$

For Channel 1 (Channel 2) a DNL of 14 % (16%) is obtained.

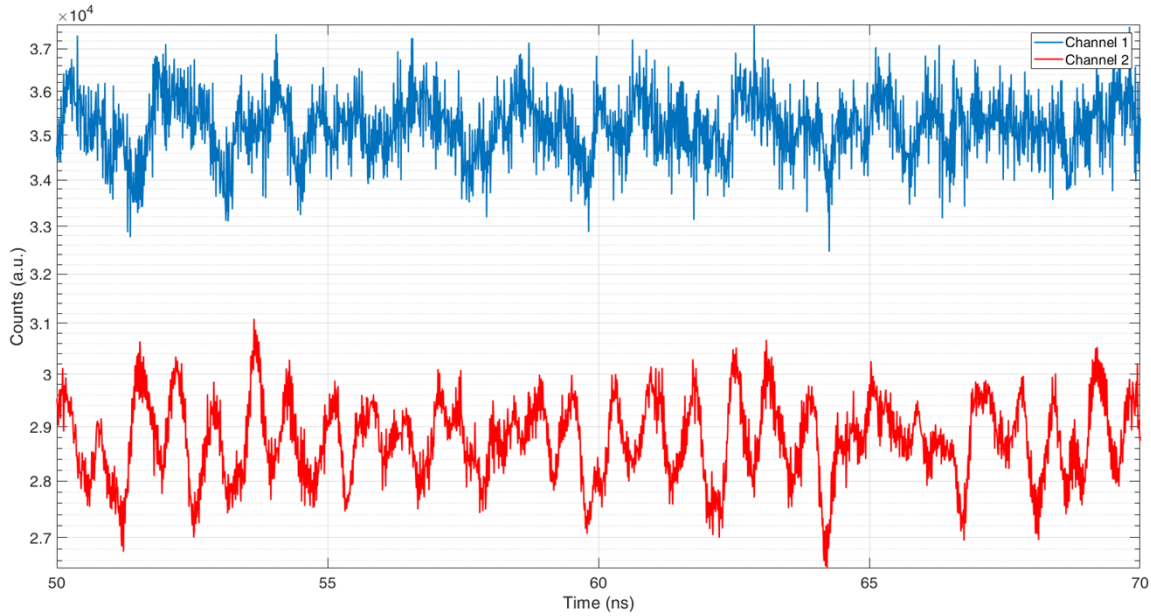

Figure 2 Signals for both Channel 1 and 2 as reconstructed by TDC 1 and 2, respectively by integrating 10 repetitions with 10 s acquisition time.

c. WHOLE SYSTEM

Instrument Response Function

The knowledge of the IRF is crucial for reconstructing properly the optical properties of the tissue under investigation. The IRF is acquired in a side-by-side configuration reaching a total photon count-rate of at least 10^6 counts/s. Its shape at each wavelength and for each channel is reported in Figure 3 after background subtraction, alongside the corresponding Full Width at Half Maximum (FWHM) in corresponding colours. The device features a temporal resolution ranging from 106 ps up to 193 ps.

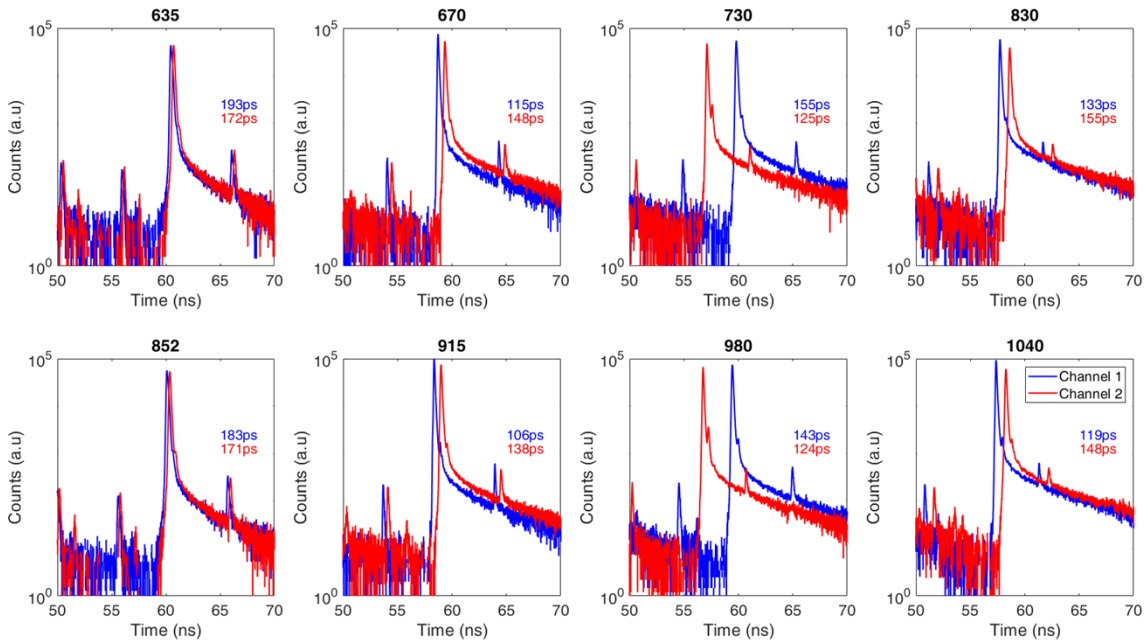

Figure 3 IRFs for Channel 1 (red curves) and 2 (blue curves) over the whole wavelength range of the TRS part of the LUCA system. For each wavelength, the time jitter (FWHM) is also reported in corresponding colours.

Stability

The stability of the entire TRS part of the LUCA device has been evaluated by placing the LUCA probe in a side-by-side IRF configuration by acquiring a TRS repetition (i.e. a full discrete spectrum) every 20 s on two different lines. This is due to the fact that, by design, every wavelength is expected to hit a target of $1 \cdot 10^6$ counts. About 190 curves per wavelength were acquired soon after switching on the device for about 1 h of stability measurement.

During the analysis, background is properly subtracted from each curve and then values of FWHM, counts and temporal position of the barycentre are computed for each channel. In particular, FWHM and barycentre temporal position are critical for model based analysis. For the sake of brevity, only results for Channel 1 for FWHM and barycentre temporal position are reported in Figure 4 and Figure 5, respectively. Similar performances are found for Channel 2. In Figure 4 the stability of the FWHM (in ps) of the IRF is reported over a period of 1 hour. Red (blue) dashed lines represent the average values ± 1 % (3%) calculated over the last 30 minutes of acquisition. After 40 minutes from switching on the device can be considered well stable, within 1% with respect to the average. Average values are represented by red continuous lines. In Figure 5 the temporal position of the barycentre is also reported. In this case red (blue) dashed lines represent the average value calculated over the last 30 minutes ± 25 (75) ps.

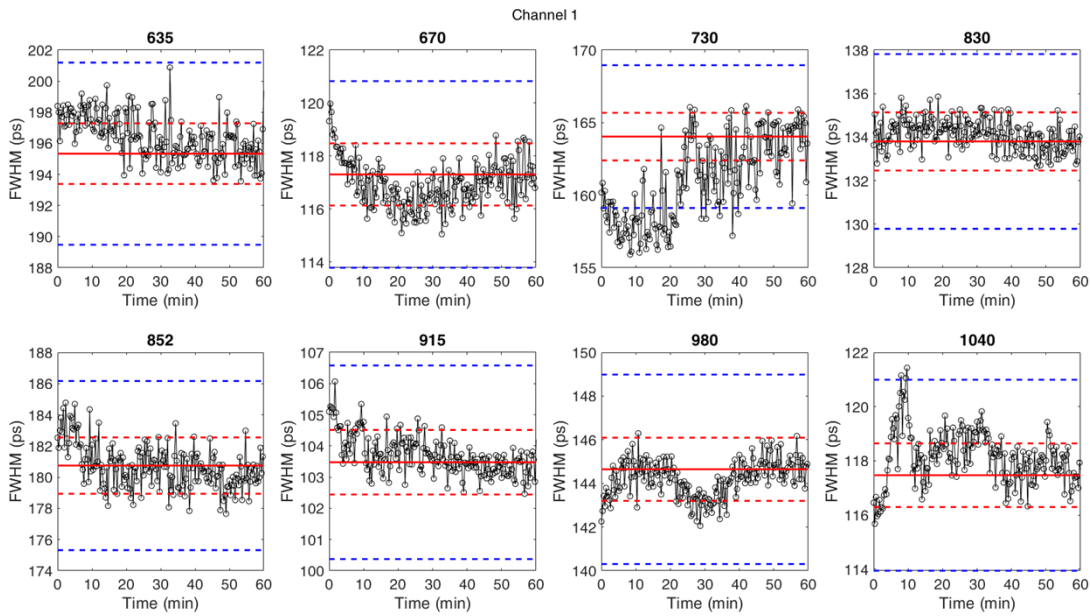

Figure 4 Stability of the FWHM of the IRF for each wavelength. Red (blue) dashed lines represent the average values ± 1% (3%) calculated over the last 30 minutes of acquisition. Average values are then represented by the red continuous lines.

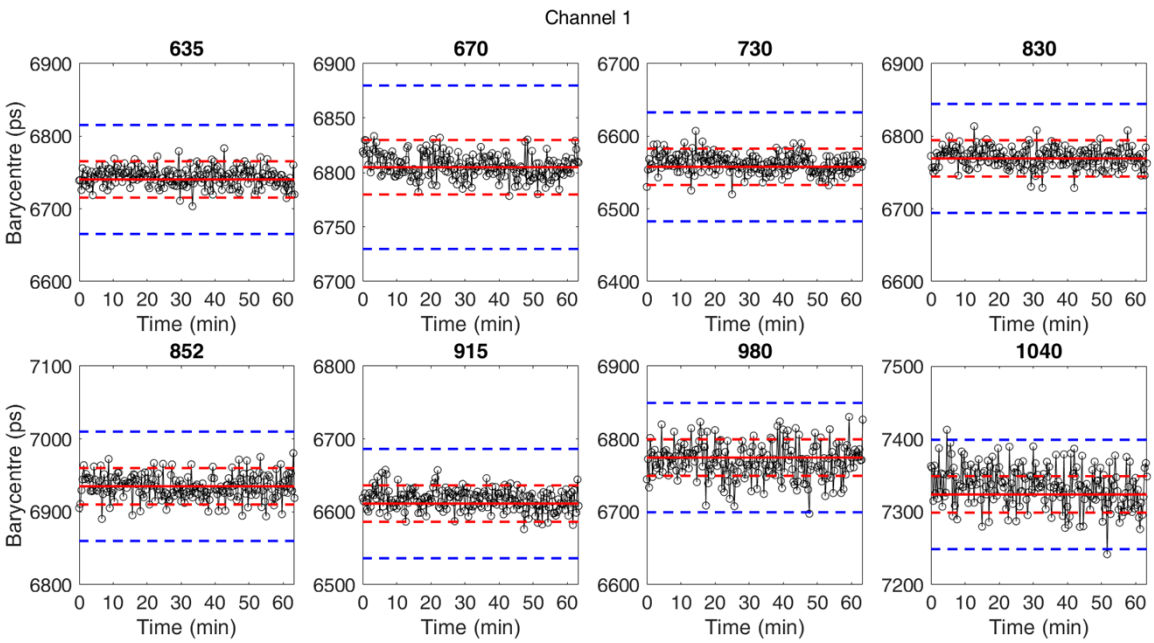

Figure 5 Stability of barycentre position in time of the IRF for each wavelength. Red (blue) dashed lines represent the average values ± 25 (± 75) ps calculated over the last 30 minutes of acquisition. Average values are then represented by the red bold continuous lines.

Afterpulsing ratio

Afterpulsing is a signal dependent noise that adds to the primary dark count-rate, increasing the overall background noise. For afterpulsing ratio calculation, we exploited responsivity measurements. An additional dark measurement was also performed.

An example of the acquired curves is shown in Figure 6. Blue curves represent the raw signal where it is possible to notice the typical decaying tail of the SiPM, which is refolded in time and it appears on the left side of the main peak. Green curves represent the signal after background subtraction.

Afterpulsing can be quantified by the figure of merit called afterpulsing ratio, calculated as follow:

$$R_{AP}(\%) = \frac{N_{mean,bkg} - N_{mean,dark}}{N_{tot}} \cdot \frac{T_{laser}}{\Delta T} \cdot 100$$

where $N_{mean,bkg}$ and $N_{mean,dark}$ correspond to the mean value of counts of the background of the acquired signal and of dark measurements, respectively. These values were computed in the region of interest delimited by the black lines in Figure 6. In the final TRS-LUCA configuration, dark measurements are acquired by stopping the laser emission by moving the optical switch on its dead channel. N_{tot} is the total number of counts of the signal after background subtraction. Finally, T_{laser} is the laser repetition period, which is in this case equal to 25 ns (40 MHz repetition rate), while ΔT is the TDC bin size (9.76 ps).

In Figure 7 the afterpulsing ratio is plotted over the entire range of wavelengths of the TRS-LUCA device. AR ranges from about 0.6 (0.7) % at 635 nm up to 8.5 (6.8) % at 1040 nm for channel 1 (channel 2). Such wavelength dependence is probably due to the contribution of the SiPM decaying tail, which is longer at longer wavelengths and affects the AR estimation. We will further investigate it, even if AR is small enough that it does not affect the reconstructed optical signal.

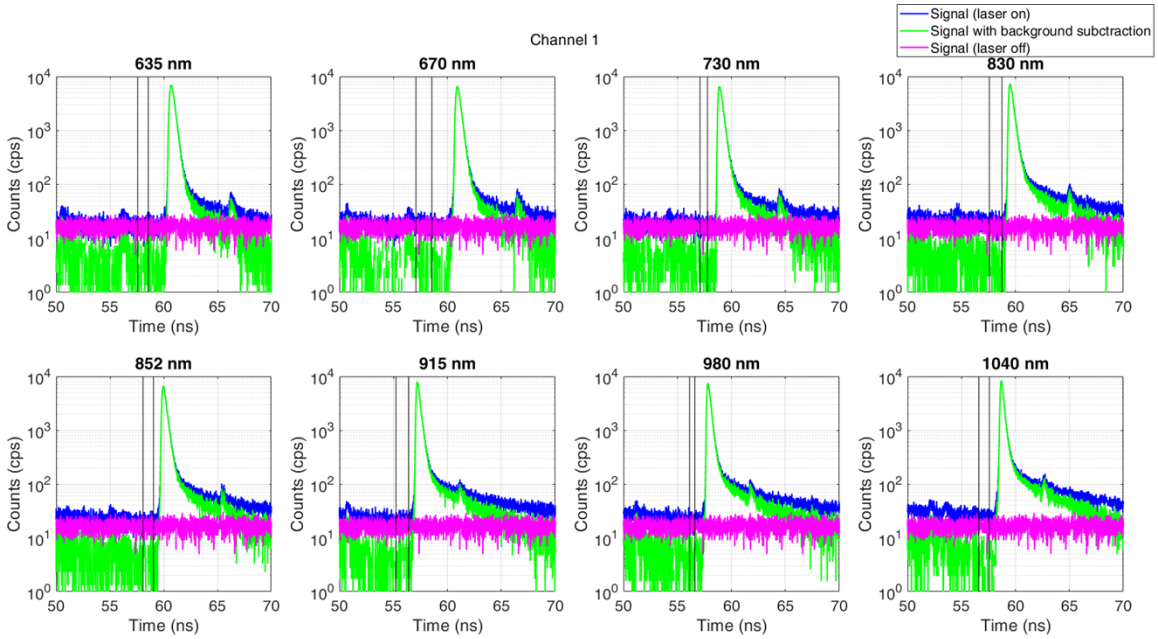

Figure 6 Acquired DTOFs for channel 1 at the 8 different wavelengths (blue curves: signal with laser emission on, green: signal with background subtraction and magenta: signal with laser emission stopped. The region of interest for background subtraction is that between vertical black lines).

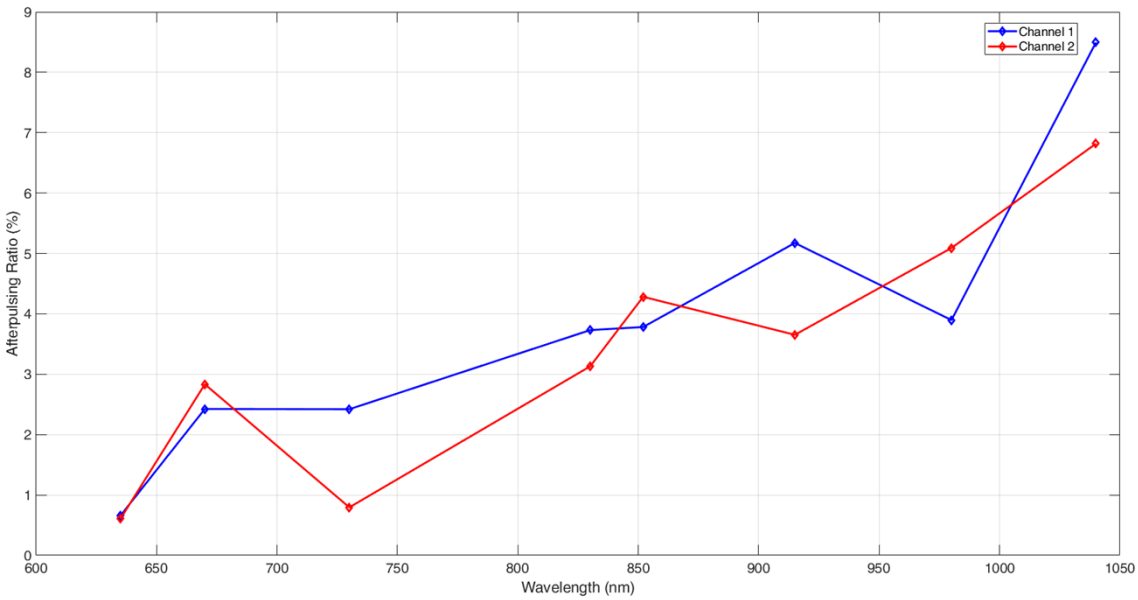

Figure 7 Afterpulsing ratio (%) plotted over the entire wavelength range for both channel 1 and channel 2.

MEDPHOT PROTOCOL:

The MEDPHOT protocol assess the capability of the device to retrieve homogeneous optical properties of the tissue/sample under investigation. As described in [2], a 32 phantom kit have been used for retrieving the linearity, accuracy and the reproducibility of the device.

This kit covers a broad range of absorption (nominal values from 0 up to 0.49 cm^{-1} in steps of 0.07 cm^{-1}) and reduced scattering (nominal values from 5 up to 20 cm^{-1} in steps of 5 cm^{-1}) [2]. In this case

measurements on absorption coefficients equal to 0 were left out since this condition is far from reality for human tissues.

a. Linearity and accuracy

For linearity measurements, 10 repetitions of 1 s time-acquisition have been acquired for each phantom. Absorption and reduced scattering coefficients were obtained by fitting the background subtracted curves with the solution of Diffuse Equation for a semi-infinite geometry. Results of linearity in absorption for both Channel 1 and Channel 2 are reported in Figure 8 and Figure 9 for each wavelength and each set of reduced scattering coefficients. Furthermore, results in linearity for reduced scattering coefficients at all the wavelengths are shown in Figure 10 and Figure 11, respectively for Channel 1 and Channel 2. For both absorption and reduced scattering coefficients, changes in the optical properties are followed linearly in both the channels. It is also possible to notice that for higher wavelengths the reduced scattering coefficient reduces in accordance with Mie's power law for scattering.

From these measurement it is also possible to evaluate the accuracy of the device which is quantified as the relative error in retrieving x_{meas} with respect the nominal value x_{nom}

$$\epsilon(\%) = \frac{x_{meas} - x_{nom}}{x_{nom}} \cdot 100$$

In this case the accuracy on average is better than 20% for the entire range of wavelengths for both absorption and scattering.

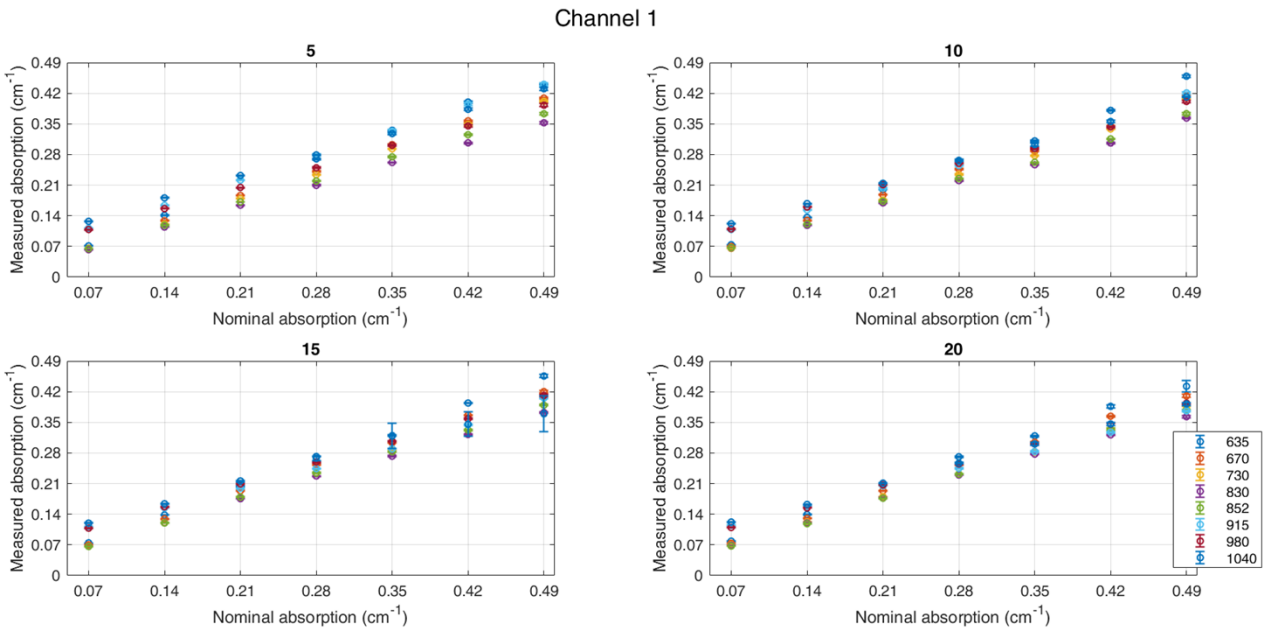

Figure 8 Measured absorption coefficient against nominal absorption coefficient (Channel 1) over the entire range of wavelengths for each scattering value set.

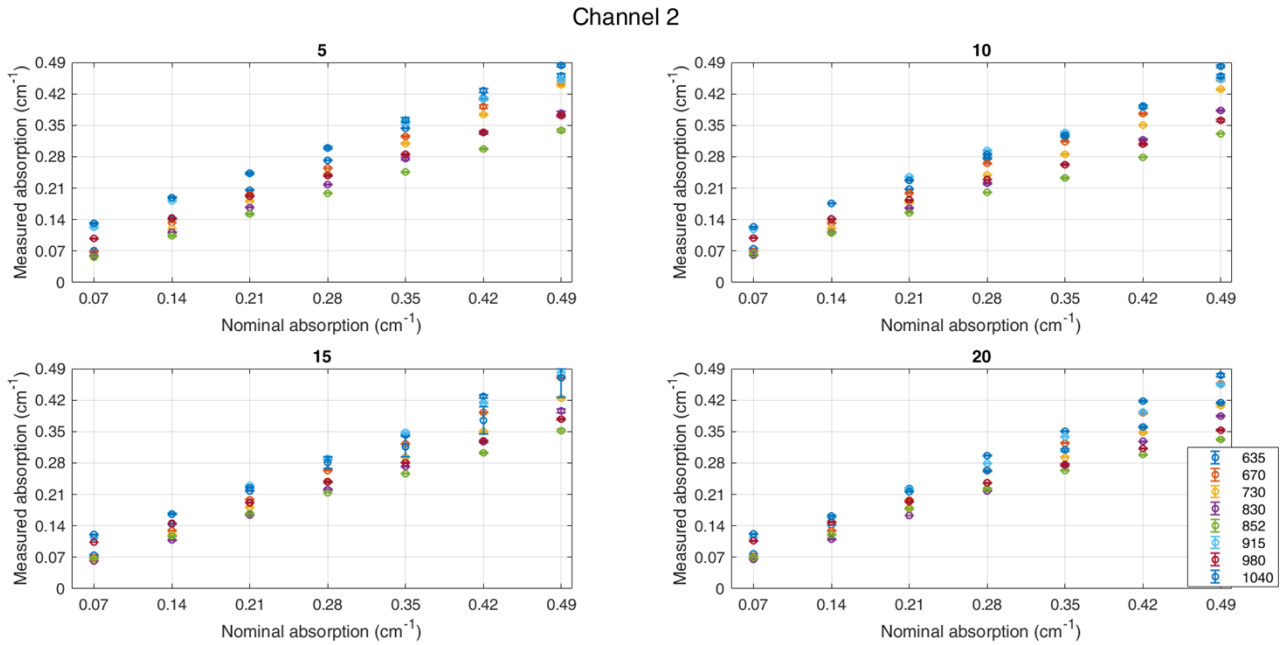

Figure 9 Measured absorption coefficient against nominal absorption coefficient (Channel 2) over the entire range of wavelengths for each scattering value set.

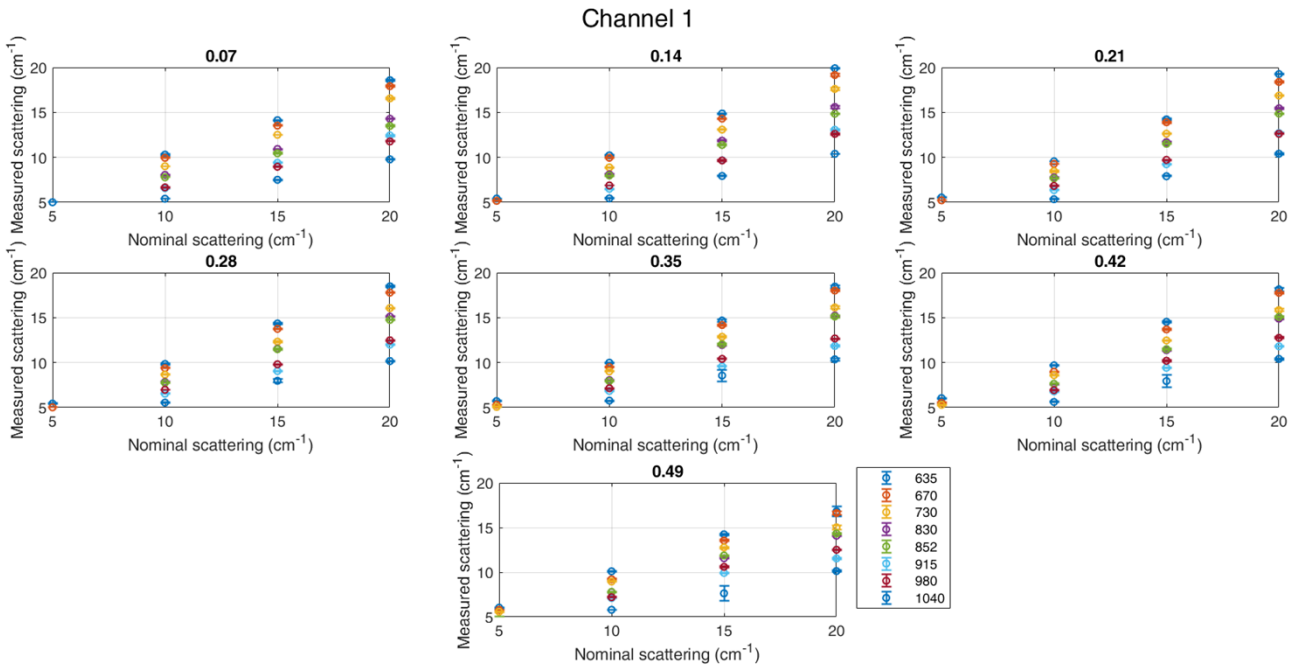

Figure 10 Measured reduced scattering coefficient against nominal scattering (Channel 1) over the entire range of wavelengths for each absorption set.

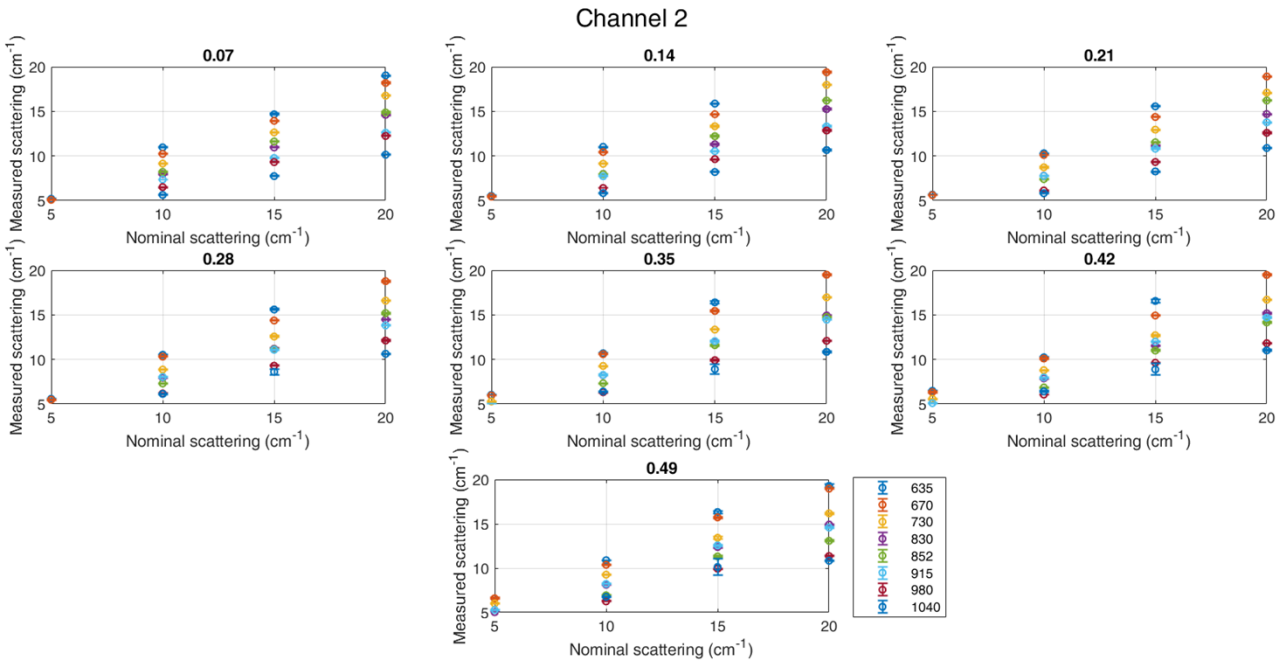

Figure 11 Measured reduced scattering coefficient against nominal scattering (Channel 2) over the entire range of wavelengths for each absorption set.

b. Noise

Noise tests assess the variability in the retrieval of absorption and reduced scattering coefficients due to random effects. With this scope, 10 repetitions were acquired on the same phantom with nominal absorption of 0.1 cm^{-1}, and reduced scattering of 10 cm^{-1} at different levels of injected light power for both channel 1 and 2. Count-rates of the signals acquired at both the SiPMs was 100 kcps, 500 kcps, 750 kcps, 1 Mcps, 1.5 Mcps and finally, 2 Mcps. For each laser power, the variation coefficient has been computed as:

$$CV\% = \frac{\sigma(x)}{\bar{x}}$$

Where x is either absorption or reduced scattering coefficient, while $\sigma(x)$ and $\bar{x}$ are the standard deviation and mean value calculated over the 10 repetitions. All the results are shown in Figure 12, Figure 13 for absorption calculation and in Figure 14 and Figure 15 for scattering. Fairly good CVs, less than 1%, are obtained for both absorption and scattering at count-rates higher than $2 \cdot 10^5$ counts per second. Dashed lines represent the best fit with a power function which highligths the dependence of CV on the power law N^n, where N is the number of counts/s. Ideally $N^{-0.5}$

corresponds to contribution of Poisson's noise to the signal. In this case n ranges from -0.4 to -0.6 in both channels.

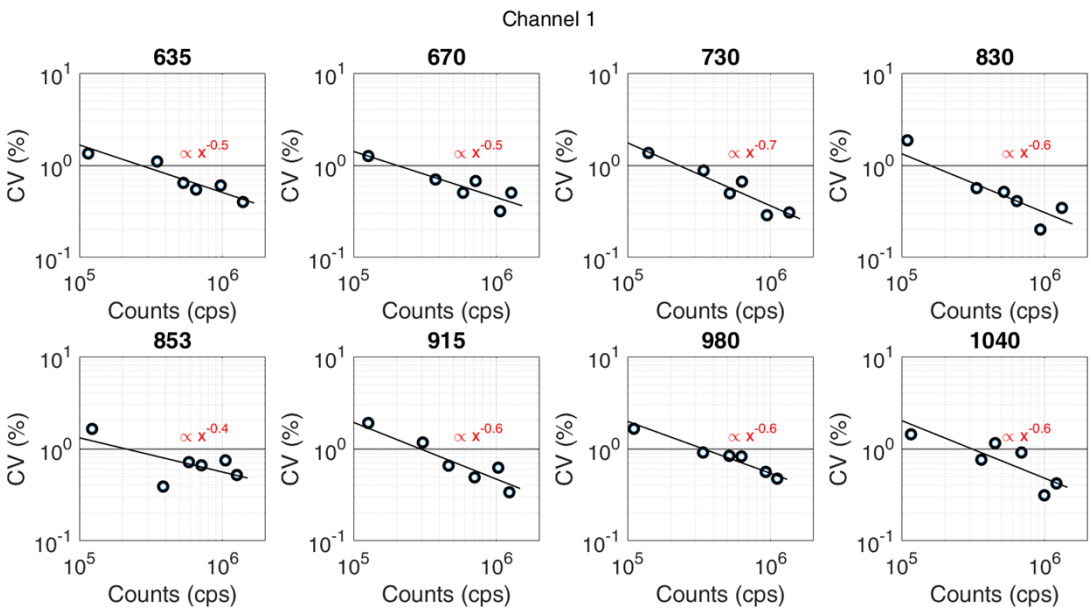

Figure 12 CV(%) for absorption at different count-rates at all the wavelengths for channel 1. CV(%) falls below a 1% threshold when a regime of about 10^5 counts per second is reached.

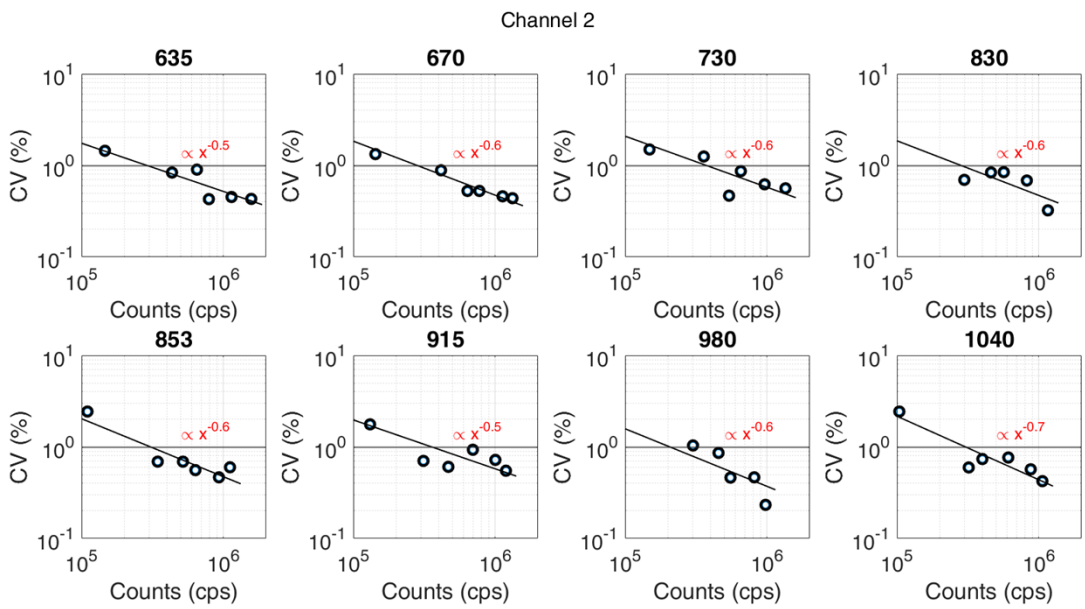

Figure 13 CV(%) for absorption at different count-rates at all the wavelengths for channel 2. CV(%) falls below a 1% threshold when a regime of about 10^5 counts per second is reached.

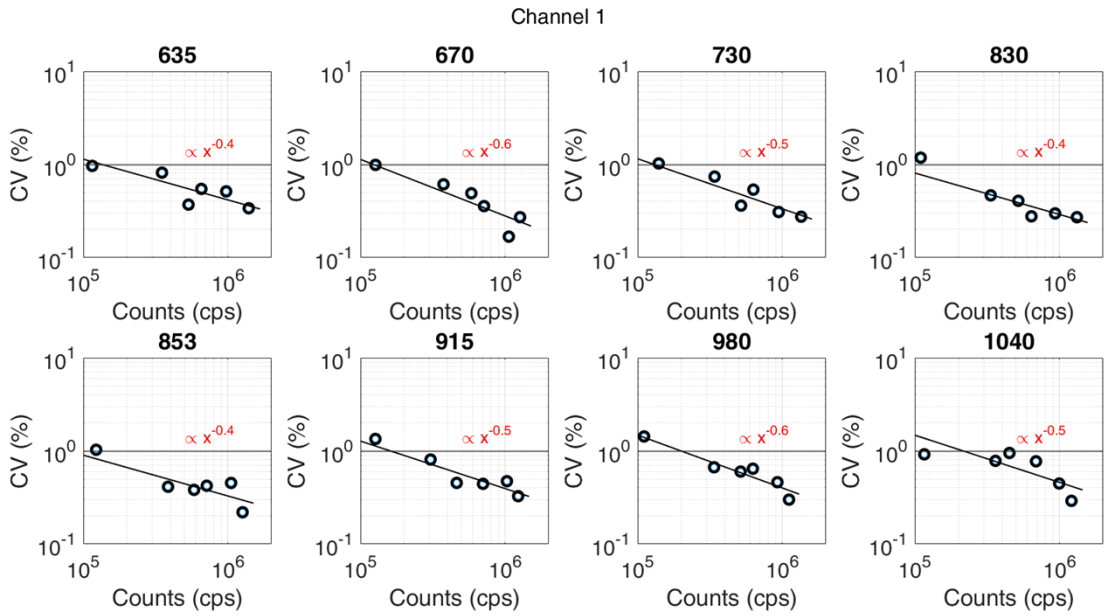

Figure 14 CV(%) for scattering at different count-rates at all the wavelengths for channel 1. CV(%) falls below a 1% threshold when a regime of about 10^5 counts per second is reached.

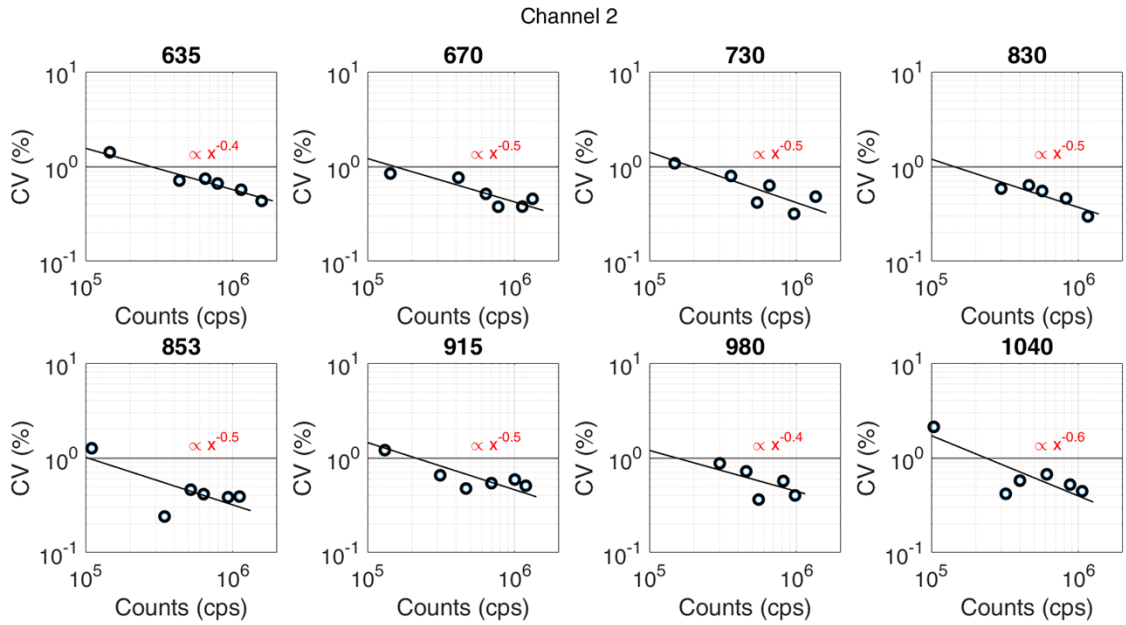

Figure 15 CV(%) for scattering at different count-rates at all the wavelengths for channel 2. CV(%) falls below a 1% threshold when a regime of about 10^5 counts per second is reached.

c. Reproducibility

Reproducibility test has been performed by repeating measurements on the same phantom (with μ_a

μ_a=0.1 cm^{-1} and μ_s' cm^{-1}), in different days. The reproducibility is expressed as the variation coefficient calculated for the retrieved absorption and reduced scattering coefficients over 3 days of measurements. Results are reported in Table 2. For absorption coefficient, the CV (%) is less than about 3% for both channels at all the wavelengths. Similarly, the CV (%) for reduced scattering coefficient is less than about 4%.

Table 2 CV (%) for absorption and reduced scattering coefficients calculated over 3 days of measurements on a phantom with with μ_a=0.1 cm^{-1} and μ_s'=10 cm^{-1}.

CV for Absorption	**635 nm**	**670 nm**	**730 nm**	**830 nm**	**852 nm**	**915 nm**	**980 nm**	**1040 nm**
Channel 1	1.46	2.04	1.59	3.04	1.63	2.73	1.62	1.49
Channel 2	1.86	2.26	2.80	1.12	2.94	3.14	2.99	2.27
CV for Scattering	**635 nm**	**670 nm**	**730 nm**	**830 nm**	**852 nm**	**915 nm**	**980 nm**	**1040 nm**
Channel 1	2.13	3.12	2.12	3.51	2.07	2.60	2.76	2.39
Channel 2	2.52	3.29	4.02	1.74	3.64	3.17	2.59	3.77

NEUROPT PROTOCOL:

NEUROPt protocol evaluates the capability of a Time-Resolved system to detect, localize, and quantify absorption changes within tissues. In this framework, small black inclusions are used to mimic absorption changes [3].

In order evaluate the detectability of localized absorption changes, we calculated the contrast as a function of the position (in step of 2 mm) of a movable rod hosted in a homogenous solid phantom (described in more details in [4]) . DTOFs were acquired in 40 different positions of the inclusion. The rod in particular is made of the same material of the homogeneous host phantom in which a small black PVC cylinder (5 mm diameter, corresponding to an absorption change of 0.17 cm^{-1} [5] and V_{inc}=100 mm^3 [6]) is inserted. We performed two scans: 1) LUCA probe is placed perpendicularly (Y scan) to the axis of the rod; 2) LUCA probe is place parallel (X scan) to the axis of the movable rod. Considering as time 0 ns the barycentre of the IRF, the contrast is calculated for 8 different time gates of 280 ps. Gating different regions of the DTOF allows us to distinguish the information obtained from early and late photons and thereby allowing us to retrieve information about deeper layer buried in the tissue (by separating the contributions from the superficial tissue). The contrast is calculated as follow:

$$C(\tau,\lambda) = -\ln\left(\frac{N(\tau,\lambda)}{N_0(\tau,\lambda)}\right)$$

where τ is the gate of the DTOF, $N_0$is the total counts of the gated DTOF acquired in the position considered as homogeneous. Finally, N is the total counts of the gated DTOF.

For the Y scan, results for both Channel 1 and 2 are shown in Figure 16 and Figure 17. For the X scan, results are shown in Figure 18 and Figure 19 for both the channels. As expected the maximum of contrast is obtained when the inclusion is below the probe (around position 30) and the value increases at later gates to finally drop due to the presence of the long constant tail of the SiPM. This is true both in scan X and Y. Differences in the maximum contrast values can be attributed to a slightly different placements of the probe with respect to Y scan. It is worth noting that in the channel 2, which correspond to a shorter source-detector distance (of about 1.85 cm) the contrast is in general slightly lower. This is due to the fact that the inclusion is placed 15 mm deep from the surface of the phantom and Channel 2 is only capable of probing more shallow perturbations.

Y scan

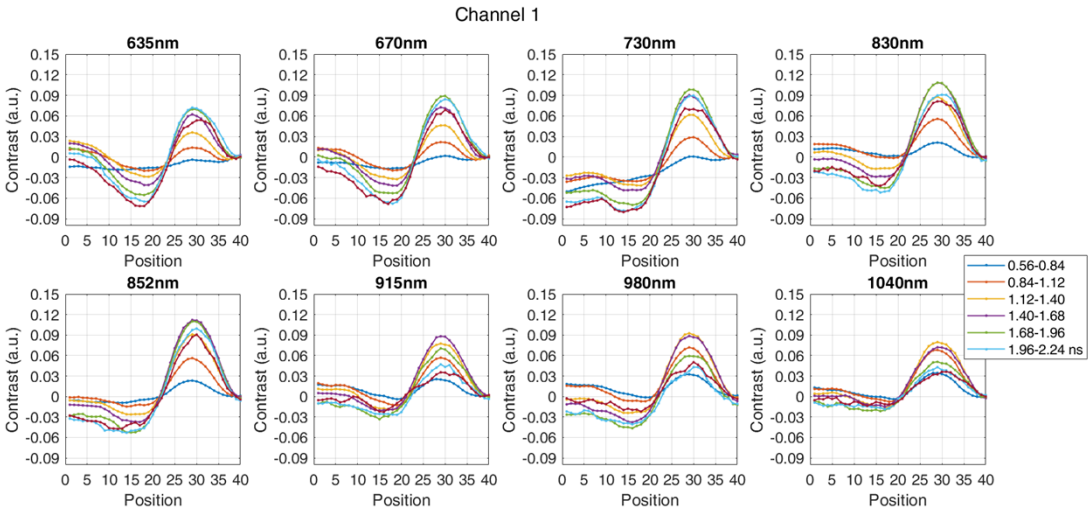

Figure 16 Y scan for Channel 1: LUCA probe is placed perpendicular to the axis of the moving rod. The contrast is plotted with respect the position of the inclusion and for different gate values of the DTOF.

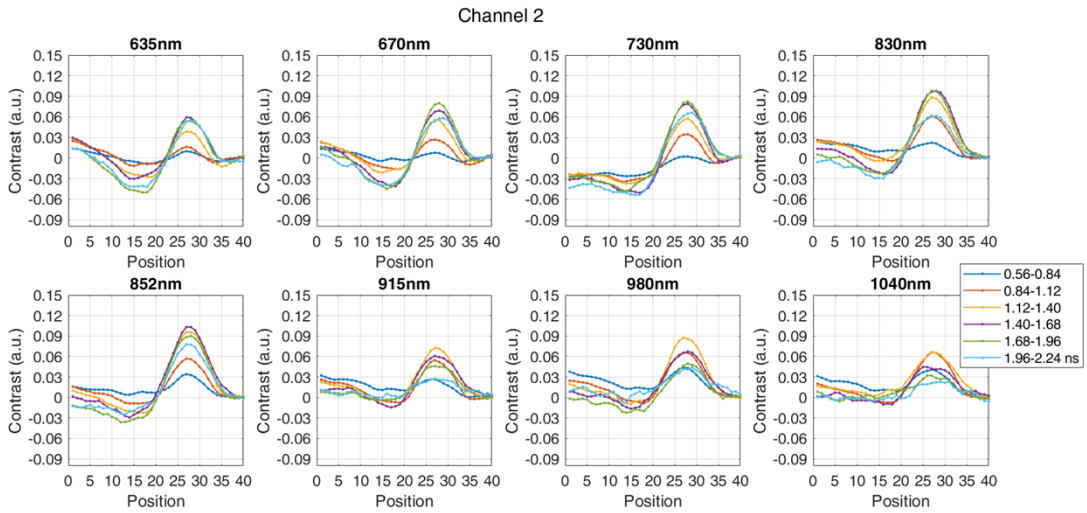

Figure 17 Y scan for Channel 2: LUCA probe is placed perpendicular to the axis of the moving rod. The contrast is plotted with respect the position of the inclusion and for different gate values of the DTOF.

X scan

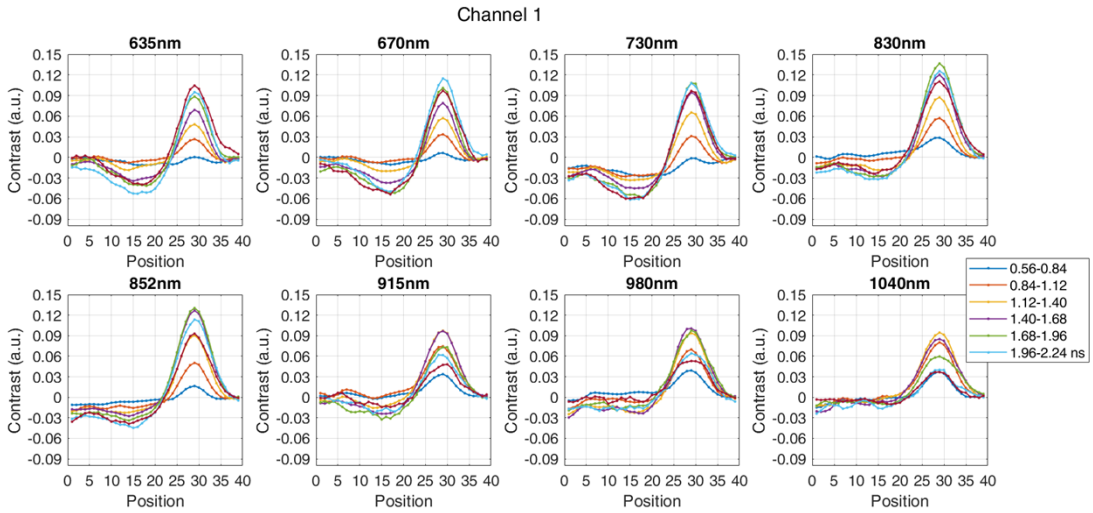

Figure 18 X scan for Channel 1: LUCA probe is placed parallel to the axis of the moving rod. The contrast is plotted with respect the position of the inclusion and for different gate values of the DTOF.

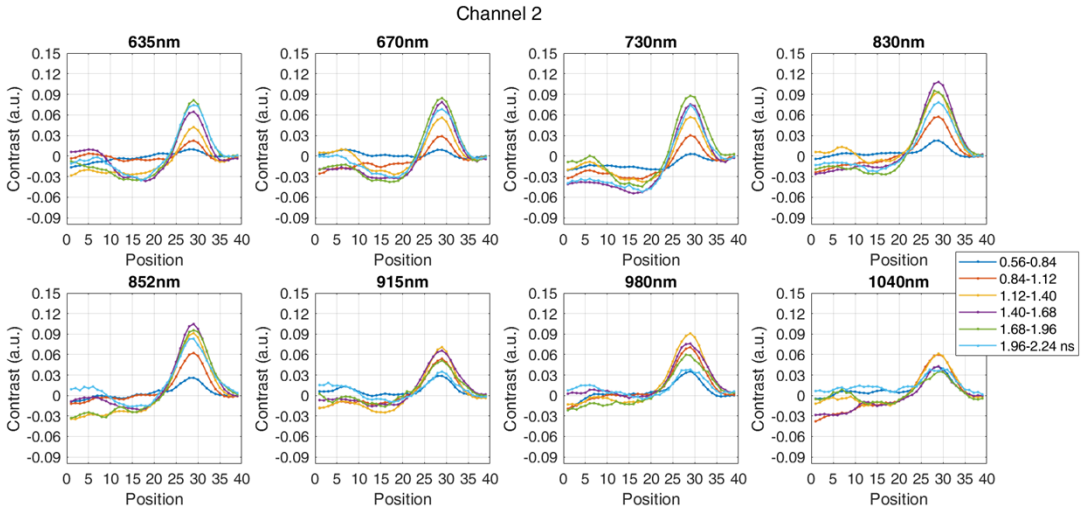

Figure 19 Y scan for Channel 2: LUCA probe is placed parallel to the axis of the moving rod. The contrast is plotted with respect the position of the inclusion and for different gate values of the DTOF.

[1] H. Wabnitz, D. R. Taubert, M. Mazurenka, O. Steinkellner, A. Jelzow, R. Macdonald, D. Milej, P. Sawosz, M. Kacprzak, A. Liebert, R. Cooper, J. Hebden, A. Pifferi, A. Farina, I. Bargigia, D. Contini, M. Caffini, L. Zucchelli, L. Spinelli, R. Cubeddu, and A. Torricelli, "Performance assessment of time-domain optical brain imagers, part 1: basic instrumental performance protocol," J. Biomed. Opt. **19**, 086010 (2014).

[2] A. Pifferi, A. Torricelli, A. Bassi, P. Taroni, R. Cubeddu, H. Wabnitz, D. Grosenick, M. Möller, R. Macdonald, J. Swartling, T. Svensson, S. Andersson-Engels, R. L. P. van Veen, H. J. C. M. Sterenborg, J.-M. Tualle, H. L. Nghiem, S. Avrillier, M. Whelan, and H. Stamm, "Performance assessment of photon migration instruments: the MEDPHOT protocol," Appl. Opt. **44**, 2140-2114 (2005).

[3] H. Wabnitz, A. Jelzow, M. Mazurenka, O. Steinkellner, R. Macdonald, D. Milej, N. Zolek, M.

Kacprzak, P. Sawosz, R. Maniewski, A. Liebert, S. Magazov, J. Hebden, F. Martelli, P. Di Ninni, G. Zaccanti, A. Torricelli, D. Contini, R. Re, L. Zucchelli, L. Spinelli, R. Cubeddu, and A. Pifferi, "Performance assessment of time-domain optical brain imagers, part 2: nEUROPt protocol," J. Biomed. Opt. **19**, 086012 (2014).

[4] A. Pifferi, A. Torricelli, R. Cubeddu, G. Quarto, R. Re, S. K. V Sekar, L. Spinelli, A. Farina, F. Martelli, and H. Wabnitz, "Mechanically switchable solid inhomogeneous phantom for performance tests in diffuse imaging and spectroscopy," J. Biomed. Opt. **20**, 121304 (2015).

[5] F. Martelli, A. Pifferi, D. Contini, L. Spinelli, A. Torricelli, H. Wabnitz, R. Macdonald, A. Sassaroli, and G. Zaccanti, "Phantoms for diffuse optical imaging based on totally absorbing objects, part 1: basic concepts," J. Biomed. Opt. **18**, 066014 (2013).

[6] F. Martelli, A. Pifferi, D. Contini, L. Spinelli, A. Torricelli, M. Mazurenka, H. Wabnitz, R. Macdonald, A. Sassaroli, P. Di Ninni, and G. Zaccanti, "Realistic inhomogeneous phantoms using an equivalent black volume," Neurophotonics, 8804 (2013).